Received: 5 November 2021 | Revised: 26 March 2022 | Accepted: 30 March 2022

High Voltage

DOI: 10.1049/hve2.12230

ORIGINAL RESEARCH

SF_6 catalytic degradation in a γ-Al_2O_3 packed bed plasma system: A combined experimental and theoretical study

Zhaolun Cui[1,2] | Chang Zhou[3] | Amin Jafarzadeh[2] | Shengyan Meng[4] | Yanhui Yi[4] | Yufei Wang[3] | Xiaoxing Zhang[3] | Yanpeng Hao[1] | Licheng Li[1] | Annemie Bogaerts[2]

[1]School of Electric Power Engineering, South China University of Technology, Guangzhou, China

[2]Department of Chemistry, Research Group PLASMANT, University of Antwerp, Antwerp, Belgium

[3]School of Electrical and Electronic Engineering, Hubei University of Technology, Wuhan, China

[4]School of Chemical Engineering, State Key Laboratory of Fine Chemicals, Dalian University of Technology, Dalian, China

Correspondence

Xiaoxing Zhang, School of Electrical and Electronic Engineering, Hubei University of Technology, Wuhan, 430068, China.
Email: xiaoxing.zhang@outlook.com

Associate Editor: Guoming Ma

Abstract

Effective abatement of the greenhouse gas sulphur hexafluoride (SF_6) waste is of great importance for the environment protection. This work investigates the size effect and the surface properties of γ-Al_2O_3 pellets on SF_6 degradation in a packed bed dielectric barrier discharge (PB-DBD) system. Experimental results show that decreasing the packing size improves the filamentary discharges and promotes the ignition and the maintenance of plasma, enhancing the degradation performance at low input powers. However, too small packing pellets decrease the gas residence time and reduce the degradation efficiency, especially for the input power beyond 80 W. Besides, lowering the packing size promotes the generation of SO_2, while reduces the yields of S-O-F products, corresponding to a better degradation. After the discharge, the pellet surface becomes smoother with the appearance of S and F elements. Density functional theory calculations show that SF_6 is likely to be adsorbed at the Al_{III} site over the γ-Al_2O_3(110) surface, and it is much more easily to decompose than in the gas phase. The fluorine gaseous products can decompose and stably adsorb on the pellet surface to change the surface element composition. This work provides a better understanding of SF_6 degradation in a PB-DBD system.

1 | INTRODUCTION

Sulphur hexafluoride (SF_6) is widely used in the power industry and the semiconductor industry due to its excellent physicochemical properties [1]. However, SF_6 is also known as a greenhouse gas, with a global warming potential (GWP) of 23,500 times that of CO_2. It's labelled as a restricted emission gas in the Kyoto Protocol [2]. In 2010, the total emission of SF_6 was about 5.32 Gg with an annual growth rate of about 10%, of which the power industry accounts for about 70% [3]. This exacerbates the detrimental effect of SF_6 on the environment.

In recent years, in order to mitigate or eliminate the environmental hazards caused by the SF_6 emission, researchers have proposed various methods for SF_6 harmless abatement. The mainstream approaches include thermal degradation [4], thermal catalysis [5, 6], photocatalysis [7, 8], electrochemical degradation [9] and plasma-assisted degradation [10]. Among them, non-thermal plasma (NTP) holds promise for SF_6 degradation and can achieve both high degradation efficiency and high energy yield, which is suitable for the industrial application [11].

NTP methods used in SF_6 abatement involve, among others, microwave discharge, radio-frequency discharge, electron beam and dielectric barrier discharge (DBD) [11]. The first three methods have relatively complex equipment and/or generate plasma with temperatures up to thousands of degrees, showing a high-volume processing capability and a relatively low energy efficiency. In contrast, a DBD is a simple device and the plasma (gas) temperature usually remains below 200°C or even at room temperature. It can easily be combined with a packing material or catalysts. In 2019, we studied the influence of the packing material type on SF_6 degradation in a packed bed DBD (PB-DBD) and found that both glass beads and

This is an open access article under the terms of the Creative Commons Attribution-NoDerivs License, which permits use and distribution in any medium, provided the original work is properly cited and no modifications or adaptations are made.

© 2022 The Authors. *High Voltage* published by John Wiley & Sons Ltd on behalf of The Institution of Engineering and Technology and China Electric Power Research Institute.

γ-Al_2O_3 pellets could promote the degradation efficiency. Additionally, γ-Al_2O_3 packing could change the SF_6 degradation pathway and regulate the product selectivity [12].

Apart from that, various studies have proven that PB-DBD plasma reactors, as a plasma-catalysis approach, show good potential in other fields, such as C1 gas conversion and volatile organic compound (VOC) abatement [13]. For instance, Shao's group investigated the conversion of CO_2 and CH_4 gases in a packed bed DBD system and found that the power supply conditions as well as the Ni-based catalysts could be important factors for the treatment [14, 15]. Wang et al. carried out plasma-catalysis experiments on CO_2 hydrogenation to methanol and achieved high conversion rate and high yield at room temperature and at atmospheric pressure [16]. Jiang et al. systematically studied the abatement of VOC gases and investigated the determining factors such as the reactor parameters and the catalyst combination [17]. Related studies have proven that the processing results are closely related to the surface properties of the packing materials. Besides, in PB-DBD applications, researchers found that the packing size acts as an important factor determining the plasma performance and the gas conversion results. For instance, Kasinathan et al found that decreasing the MO_x (Al_2O_3) (M = Ti and Mg) catalyst size can promote the conversion of methane [18]. In 2016, Butterworth et al found that the packing size of packing materials plays an important role in CO_2 reduction and significantly impacts the discharge characteristics [19]. In 2021, Wang et al demonstrated that increasing the size of ceria zirconia Ni-based catalysts leads to higher CO_2 conversion and better plasma homogeneity [20]. Nevertheless, there is a lack of investigation for the size effects and surface properties of the packing size on SF_6 degradation. The influence and mechanism of γ-Al_2O_3 packing with different sizes on the degradation efficiency and the product selectivity are unclear.

Therefore, to further investigate the packing effects of γ-Al_2O_3 on SF_6 degradation, we carried out a combined experimental and theoretical study. 1, 2, and 4 mm diameter γ-Al_2O_3 pellets are tested as the packing material, and their effect is investigated on both the discharge behaviour and degradation efficiency. Characterisation tests are made to study the dependence of SF_6 degradation on the surface properties of the pellets. Density functional theory (DFT) calculation is applied to analyse how SF_6 adsorbs and decomposes on the γ-Al_2O_3 pellet surface and the formation of surface fluorine species. Overall, these findings contribute in several ways to our understanding of the effects of the packing material size and surface properties on SF_6 degradation, thus providing a basis for the SF_6 harmless abatement by a PB-DBD plasma.

2 | METHODS

2.1 | Experimental setup and degradation parameters

The experimental setup has been described in our previous study [12] and is shown in Figure 1. In this experiment, the discharge frequency is maintained at 8.5–9.0 kHz and input power is controlled within 100 W. We selected argon (Ar) as the background gas for SF_6 dilution due to its promotion effects on the discharge and SF_6 degradation [21]. The standard gases of Ar and SF_6 are in high purity of 99.99%, and they are mixed to a certain proportion by a gas sample compounder. The discharge voltage and current signals are recorded by the oscilloscope (Tektronix MSO44). Other discharge parameters such as the capacitance of the dielectric C_{diel}, total capacitance of the reactor C_{cell}, effective capacitance of the dielectric during the discharge ζ_{diel} and discharge-off coefficient alpha (α) are obtained and calculated from the Q-V plot [22, 23].

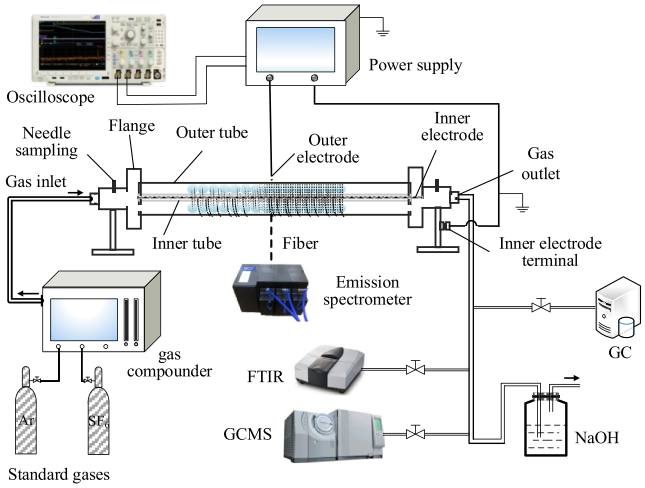

FIGURE 1 Schematic diagram of the experiment setup

After the degradation, the SF_6 concentration is detected by a gas chromatograph (GC) (Kejie GC8900) and the gas products are qualitatively analysed by Fourier transform infrared spectroscopy (FTIR) (Thermo iS50). All the peak characteristics and diagnosis of SF_6 products are based on the work of Kurte et al [24]. Subsequently, four stable products, that is, SOF_4, SOF_2, SO_2F_2 and SO_2, are quantitatively detected by gas chromatography–mass spectrometry (GCMS) (Shimadzu QP2020-NX).

There are three main factors to determine the degradation performance: destruction and removal efficiency (DRE), energy yield (EY) and product selectivity.

The DRE can be calculated by equation (1):

$$DRE = \frac{C_{in} - C_{out}}{C_{in}} \times 100\% \tag{1}$$

where C_{in} and C_{out} are the initial and final concentrations of SF_6, respectively.

The EY at a certain condition is calculated using equation (2):

$$EY = \frac{M_{SF_6}}{P \times t} \tag{2}$$

where M_{SF_6} is the mass of degraded SF_6 in units of gram (g). p is the input power in units of watt (W). t is the degradation time. The unit of EY is g/kWh.

After the degradation, the selectivity of four stable products (SOF_4, SOF_2, SO_2F_2 and SO_2) can be calculated by equation (3):

$$S_X = \frac{C_x}{C_{sum}} \times 100\% \quad (3)$$

where C_x and C_{sum} are the concentrations of product x and the total concentration of these four gases.

2.2 | Catalyst characterisation

X-ray diffraction (XRD) patterns of catalysts are recorded using a Rigaku D-Max 2400 diffractometer with Cu Kα radiation. Nitrogen physisorption is conducted on a Micromeritics ASAP 3020 instrument (Micromeritics, Atlanta, USA) at −196°C to obtain textural information. Before the measurement, the samples (0.15 g) are degassed at 350°C for 4 h. The surface area is determined based on the Brunauer–Emmett–Teller (BET) method, and the pore volume is calculated by the t-plot method at a P/P0 = 0.99. X-ray photoelectron spectroscopy (XPS) is carried out using a VG ESCALAB MK2 spectrometer to reveal the chemical environment of the elements in the catalysts. SEM images are taken on a FlexSEM-1000 instrument (Hitachi). Before the characterisation, the spent Al_2O_3 pellets samples are treated for 3 h.

2.3 | Computational details

To study the surface catalytic properties of the γ-Al_2O_3 pellets, we carried out DFT calculations using the CP2K Quickstep package [25]. The Gaussian and plane wave method (GPW) is applied with the Goedecker–Teter–Hutter (GTH) pseudopotentials [26]. The cutoff value for the plane wave methods is 600 Ry. The generalized-gradient approximation by Perdew-Burke-Emzerhof functional methods is chosen to describe the exchange correlation functional with the DFT-D3 method for the dispersion correction [27, 28]. The geometry optimisation is calculated by Broyden–Fletcher–Goldfarb–Shanno (BFGS) strategy and the transition state (TS) of the S–F bond-breaking reaction is carried out by the climbing image nudged elastic band (CI-NEB) method [29, 30]. In this study, the γ-Al_2O_3(110) is selected as the typical pellet surface [31]. We built the γ-Al_2O_3(110) model by a 2 × 2 supercell, with the XYZ dimensions of 16.1439 × 16.7874 × 40.0000 $Å^3$.

The adsorption energy E_{ad} for the surface molecules is calculated by equation (4):

$$E_{ad} = E_{gas+slab} - E_{gas} - E_{slab} \quad (4)$$

where E_{gas} and E_{slab} are the energy of gas molecules and of the slab, respectively, and $E_{gas+slab}$ is the total energy of the system after the adsorption.

3 | RESULTS AND DISCUSSION

3.1 | Discharge parameters

Figure 2 shows the size effect of the packing on the discharge voltage and current at 80 W input power. The voltage and current amplitudes are similar in the three systems, with maxima around 14 kV and 30 mA, respectively. The 1 mm system has the most abundant filaments in its current signal and the number of filaments decreases with increasing packing size. In the 4 mm system, the filaments are even not clear. The discharge images are shown in Figure S1, where the 1 mm packing system shows the most intense discharges. This result demonstrates that a smaller size packing has a more typical packed bed effect, which is attributed to the sharper edges and contact points in the gap [32]. The abundant micro-discharges in the smaller pellet packing reactor could facilitate the formation of plasma species, resulting in a more efficient degradation of SF_6. Besides, we summarised the discharge voltage and the discharge power along with the input power in Figure 3. In Figure 3a, at 50–80 W input powers, the voltage distributions in the three systems are very close. When the input power exceeds 80 W, the voltage in the 4 mm system grows less significantly than in the other two systems as a function of power. This indicates that the large size may have a negative effect of the discharge voltage. In Figure 3b, the discharge power distributes similarly in each system, lying in the order of 2 mm > 1 mm > 4 mm.

Typical Q-V plots of the three packing systems at 80 W are shown in Figure 4. Varying the packing size affects the shape of the Q-V plots. It is clear that the slopes of the AB and DC lines, as well as the charge peak-peak value $Q_{pk\text{-}pk}$ increase with decreasing packing size. This indicates that the small size packing increases the effective dielectric capacitance ζ_{diel} and enhances the charge transfer process. Moreover, the changes of the effective dielectric capacitance ζ_{diel} and the α values along with the input power are shown in Figure 5. However, in Figure 5a, the ζ_{diel} values decrease with increasing packing size, especially for the 4 mm system. In general, the size change has a limited effect on discharge power but a significant impact on the ζ_{diel} distribution. In Figure 5b, the α coefficient in the 4 mm system is obviously larger than the other two systems, corresponding to a larger discharge-off proportion in one DBD cycle. It means that decreasing the packing size yields a more fully discharge and slightly increases the discharge power, which improves the ignition and the maintenance of the plasma.

3.2 | Degradation performance

3.2.1 | DRE and energy yield

As shown in Figure 6, the values of DRE and EY in the three packing systems are plotted against the input power. In Figure 6a, DRE increases rapidly with the input power in the

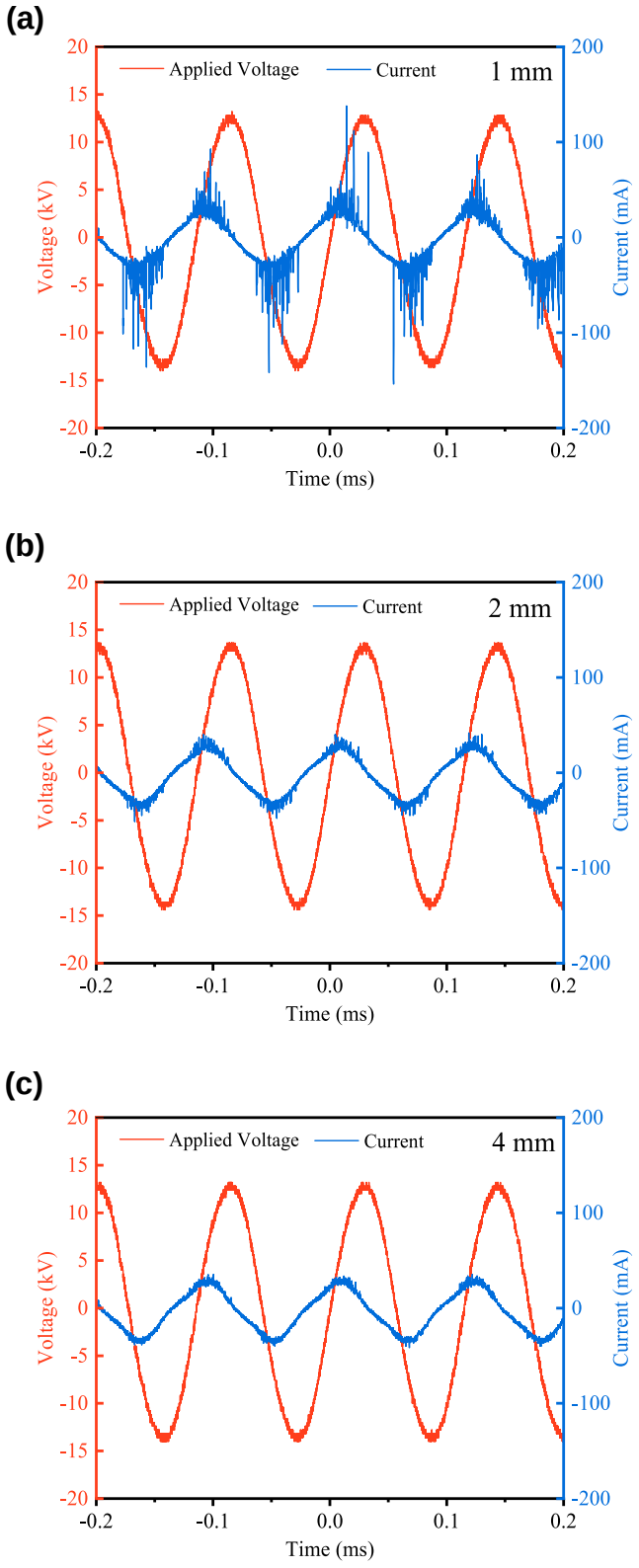

FIGURE 2 Discharge voltage and current signals in three discharge systems (3% SF_6–97% Ar, 100 mL/min, 80 W input power). (a) 1 mm, (b) 2 mm,and (c) 4 mm

range of 50–80 W and then shows a slow growth at 90 and 100 W. Among the three sizes, the 2 mm system shows the highest DRE distribution at the range of 60–100 W. The DRE

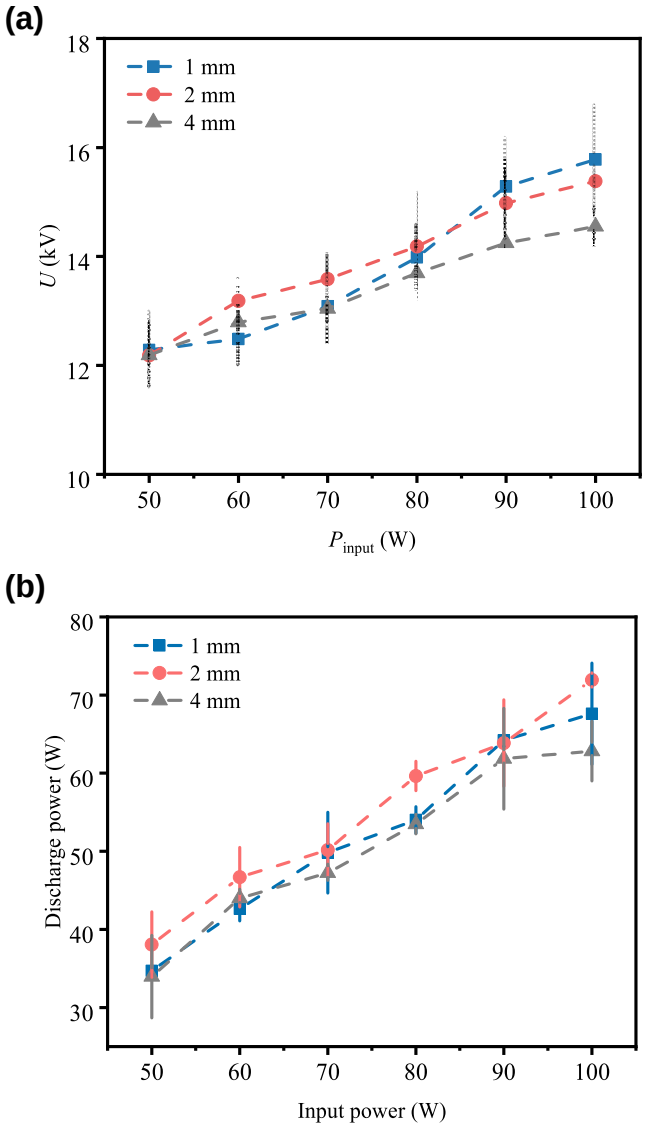

FIGURE 3 Discharge voltage amplitude and discharge power as a function of the input power (3% SF_6–97% Ar, 100 mL/min, 80 W input power). (a) Discharge voltage amplitude and (b) discharge power

of 1 mm is higher than the 4 mm packing at a low power range (50–80 W) and is lower at 90 and 100 W. The gas residence time in the discharge region for a packing of 1, 2 and 4 mm is 3.31, 4.59 and 6.96 s, respectively. It could be speculated that when the input power is high enough, all three packing systems have an intensive discharge for SF_6 degradation, and then the gas residence time could be a main factor to determine the DRE. Therefore, the DRE in the 4 mm system is higher than that in the 1 mm system and reaches close to the 2 mm system. In Figure 6b, the EY values first increase and then decrease with the input power increasing. The 80 W is the turning point because the DRE barely increases beyond this power. Likewise, the 2 mm system shows the highest EY distribution, that is, 13.45 g/kWh at 80 W and gradually drops to 11.31 g/kWh at 100 W. The better performance of the 2 mm packing system could be attributed to a proper balance among the residence time, the contact area and the discharge intensity.

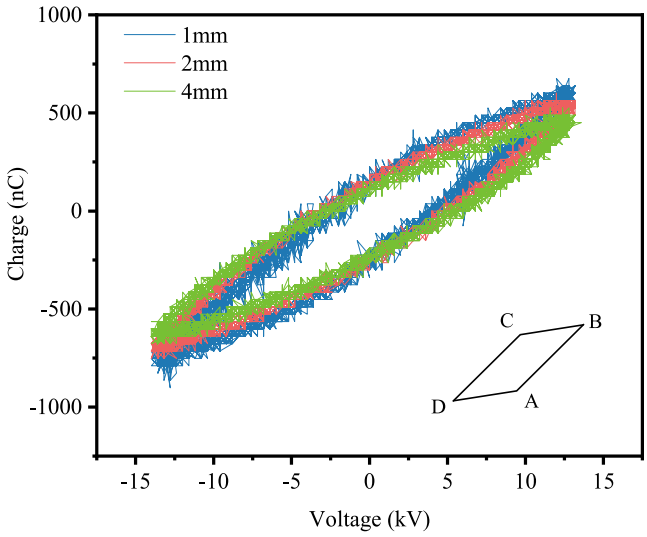

FIGURE 4 Lissajous figures of the three packing systems at 80 W input power (100 mL/min, 3% SF_6–97% Ar)

To further evaluate the degradation performance, we studied the DRE and EY as a function of the gas flow rate, as shown in Figure 7. In Figure 7a, the input power is fixed at 80 W and the DRE decreases with the increasing flow rate. The 2 mm system has the highest DRE distribution, which decreases from 93.15% at 100 mL/min to 79.13% at 300 mL/min. The DRE values of 1 and 4 mm are very close, and they drop from about 90% at 100 mL/min to about 50% at 30 mL/min. In Figure 7b, the EY increases with the flow rate. The EY values and the growth rate of the 2 mm system are obviously larger than that in the other two systems, which increases from 13.45 g/kWh at 100 mL/min to 34.82 g/kWh at 300 mL/min. It is clear that increasing the flow rate makes more SF_6 molecules pass through the plasma region to have a decomposition per unit time, eventually resulting in a higher EY. Besides, the EY values of 1 and 4 mm show a saturation with the increasing flow rate, but this is not observed in the 2 mm system, indicating a potential for the 2 mm system to treat higher flow rates or higher concentrations of SF_6 gas.

3.2.2 | Product analysis

The FTIR results of the three packing systems are summarised in Figure S2. The main products are SOF_4, SOF_2, SO_2F_2, SO_2, SiF_4, SF_4, and S_2F_{10}, which are typical DBD degradation products, as shown in a previous study [11]. Among them, SiF_4 is generated by the reaction between F atoms and SiO_2 from the quartz tube surface. SF_4 and S_2F_{10} are primary degradation products generated from the S–F bond-breaking and SF_x combinations. They are unstable and can further decompose or react with other species [33]. SOF_4, SOF_2, SO_2F_2 and SO_2 are stable products in the tail gas. In this study, there is no obvious SOF_4 peak in either 1 or 2 mm systems, which may be caused by its further decomposition. Moreover, the 1 mm system shows the highest SO_2 peak and the lowest peaks of SOF_2

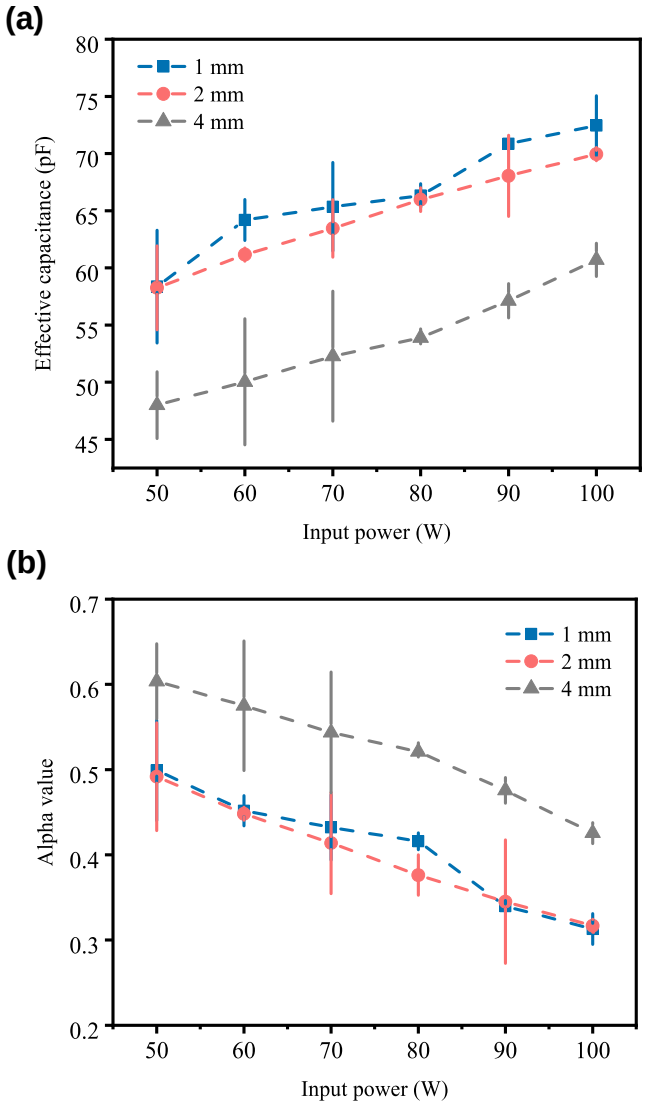

FIGURE 5 Effective dielectric capacitance ζ_{diel} and alpha value (α) as a function of the input power (3% SF_6–97% Ar, 100 mL/min, 80 W input power). (a) Effective dielectric capacitance ζ_{diel} and (b) alpha value (α)

and SO_2F_2, which means the product selectivity is affected by the size variation. Therefore, we present the distribution of the selectivity of the four stable products as a function of the packing size as well as the input power, as shown in Figure 8.

In Figure 8a, it is clear that increasing the packing size reduces the SO_2 selectivity, while it promotes the yields of the other three gases. In the 1 mm system, SO_2 is the most abundant product with a concentration and selectivity of 5319 ppm (part per million, volume fraction) and 68.29%, respectively. The concentrations and the selectivity of SO_2F_2 and SOF_2 are 2125 and 343 ppm, and 27.28% and 4.40%, respectively. In the 2 and 4 mm systems, the SO_2F_2 yield is the highest, and the concentration and selectivity are 4610 and 5758 ppm, 54.71% and 77.33%, respectively, while the SO_2 selectivity decreases to 40.56% and 10.89%, respectively. The SOF_2 selectivity is similar in the 1 and 2 mm systems, at around 4.7%, while it increases to 11.11% in the 4 mm system. There is almost no SOF_4 in the

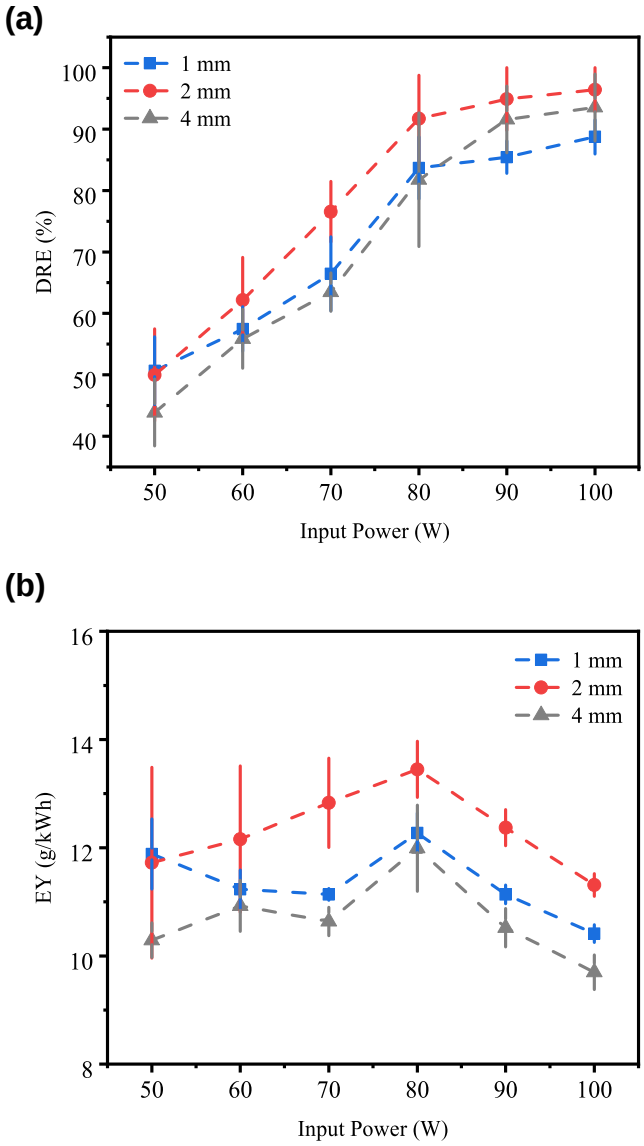

FIGURE 6 The DRE and energy yield (EY) distributions in three packing systems as a function of the input power (3% SF_6–97% Ar, 100 mL/min). (a) DRE and (b) EY

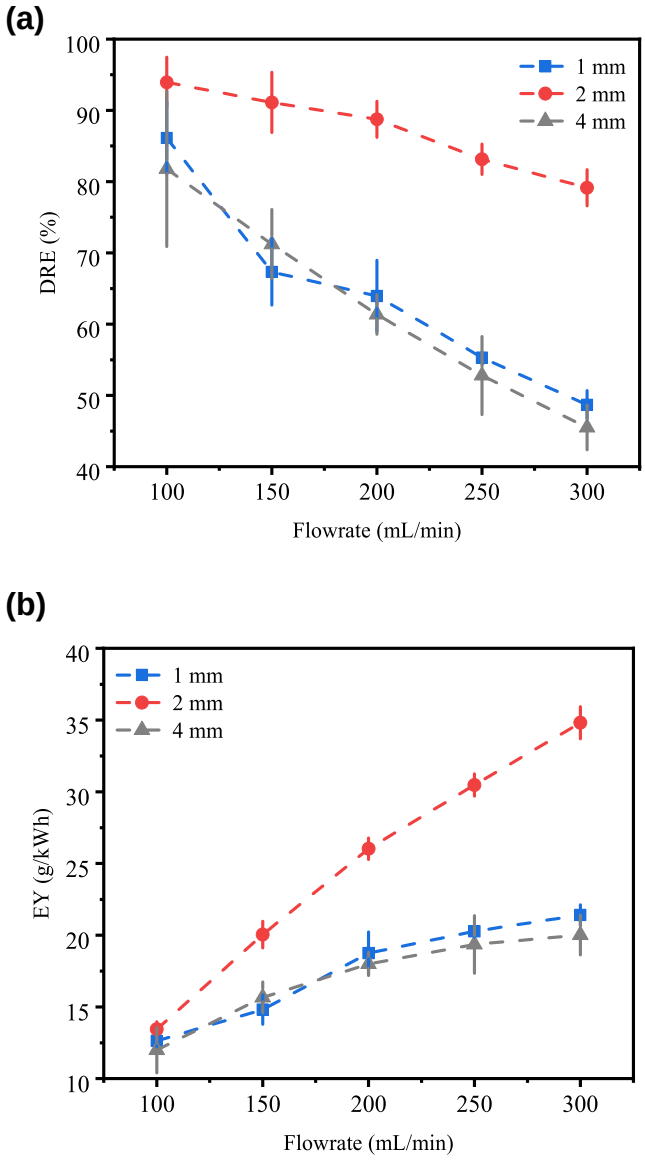

FIGURE 7 The DRE and energy yield (EY) distributions in the three packing systems as a function of the flow rate (3% SF_6–97% Ar, 80 W). (a) DRE and (b) EY

1 mm or the 2 mm systems, and SOF_4 exists at a very low selectivity of 0.67% in the 4 mm system. Zhong et al found that SO_2 is a final product generated by some further reactions of the S-O-F products during SF_6 degradation [34]. Therefore, it could be speculated that SOF_4 in this study acts as an intermediate, which is subject to further degradation.

In Figure 8b, we selected the 2 mm system to study the effects of the input power on the product selectivity. The selectivity of SOF_2 and SO_2F_2 decreases, while the SO_2 selectivity increases with the input power. Interestingly, SO_2F_2 has the highest selectivity at a low power range from 50 W up to 80 W, while the SO_2 selectivity is the highest at 90 and 100 W. In detail, the SO_2F_2 concentration and selectivity change from 3858 ppm to 87.94% at 50 W, to 4609 ppm and 54.71% at 80 W, and eventually drops to 3114 ppm and 33.06% at 100 W. In contrast, the SO_2 concentration and selectivity are only 282 ppm and 6.43% at 50 W, and they finally increase to 6154 ppm and 65.31% at 100 W. Besides, in Figure 6a, the DRE hardly changes in the 2 mm system beyond 80 W, but the product distribution changes obviously from 80 to 90 W in Figure 8b. This indicates that a further conversion of SO_2F_2 occurs with increasing input power.

In general, a more intensive discharge and a large contact area of the pellets account for more efficient decomposition of SF_6, resulting in a larger selectivity of SO_2. It should be noted that the percentage of the four stable S-containing gases in decomposed SF_6 decreases with the input power, from about 49% to 36%. Apart from the primary products such as SF_x, the other S-based and F-based products may be in solid form on the pellet surface. This is indeed proven by XPS shown in section 3.3.

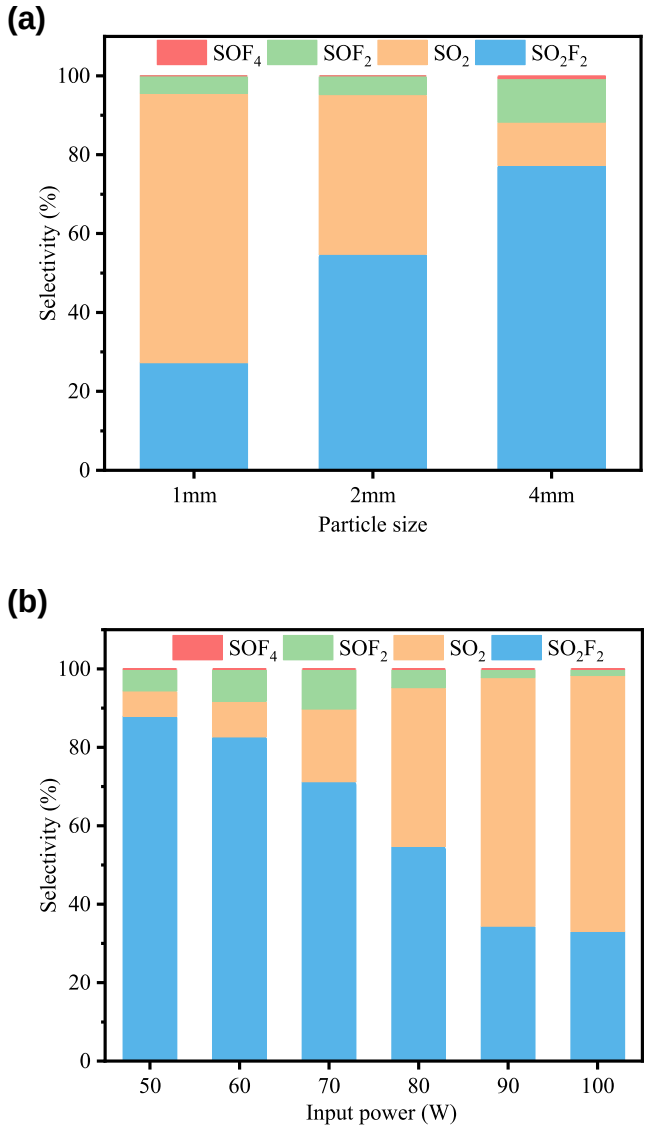

FIGURE 8 Distribution of the selectivity of the four main products. (a) With three packing sizes (3% SF_6–97% Ar, 80 W, 100 mL/min) and (b) as a function of the input power (3% SF_6–97% Ar, 80 W, 2 mm packing)

It should be noted that most of the plasma degradation products are toxic and can be effectively adsorbed by an alkaline solution except SO_2F_2 [11]. SO_2F_2 has a relatively strong stability and has a solubility of 0.2% in water. Multiple methods and specific adsorbents are needed to treat this gas. Therefore, lowering the selectivity of SO_2F_2 is beneficial to the SF_6 tail gas recycle in terms of process and economics. This study proves that utilising small size pellets and high input power can both reduce the SO_2F_2 production and increase the SO_2 yield.

3.3 | Characterisation of the γ-Al_2O_3

The isotherms of γ-Al_2O_3 show type IV characteristics in Figure S3, indicating that the samples have a mesoporous structure. The BET specific surface area, pore volume and pore diameter of the γ-Al_2O_3 pellets are shown in Table 1. S_{BET} is the specific surface area of the solid particle and the V_{total} is the total pore volume per unit mass of the solid particle. All three size pellets have similar surface area and pore diameter. The slight decrease in the BET surface area and pore volume of the γ-Al_2O_3 pellets after plasma treatment may be attributed to the modification of the surface by S and F.

TABLE 1 BET results of the Al_2O_3 pellets before and after the discharge

Samples	S_{BET} ($m^2 \cdot g^{-1}$)	V_{total} ($cm^3 \cdot g^{-1}$)	Pore diameter (nm)
1 mm fresh	295.1	0.41	5.9
1 mm spent	277.9	0.38	5.7
2 mm fresh	293.1	0.41	5.6
2 mm spent	273.2	0.39	5.6
4 mm fresh	293.3	0.44	6.1
4 mm spent	278.6	0.43	6.2

TABLE 2 Surface element components (except C) of the spent Al_2O_3 pellets by X-ray photoelectron spectroscopy (XPS) tests

Element	Al	O	F	S
Component rate (%)	33.42	62.93	3.16	0.49

After 3 h degradation, the 2 mm Al_2O_3 pellets were characterised by XRD and XPS tests, as shown in Figures S4 and S5. In Figure S4, the diffraction peaks of Al_2O_3 did not change obviously before and after reaction, indicating that the structure of the samples remains stable under plasma condition. The element distribution is calculated from Figure S5 and is shown in Table 2. After the degradation process, 3.16% F and 0.49% S appear at the 2 mm sample surface, indicating that the pellet surface participates in the reactions. The appearance of 29.12% C is caused by the detection method [35]. Figure 9 shows the SEM images of the fresh and spent Al_2O_3 pellets. After the discharge, the Al_2O_3 pellets become smoother and this could be one reason for the reduction of the surface area.

Overall, the catalyst characterisations prove that the discharge and degradation process affect the Al_2O_3 pellets. The surface area and appearance changed after the discharge. The degradation products could interact with the surface atoms to form some surface species, especially for the F element. In other studies, gases such as H_2O vapour and O_2 are often added to promote the degradation, which could also have impact on the pellet surface [11]. Therefore, the surface stability should be carefully evaluated at different conditions before a long-term use. This is beyond the scope and is not discussed in this work.

3.4 | SF_6 adsorption and initial bond-breaking over γ-Al_2O_3 (110) surfaces

Figure S6 shows the typical sites on a perfect γ-Al_2O_3(110) surface. As we use the 2 × 2 supercell, the adsorption sites are mainly selected in the centre of the model for a better

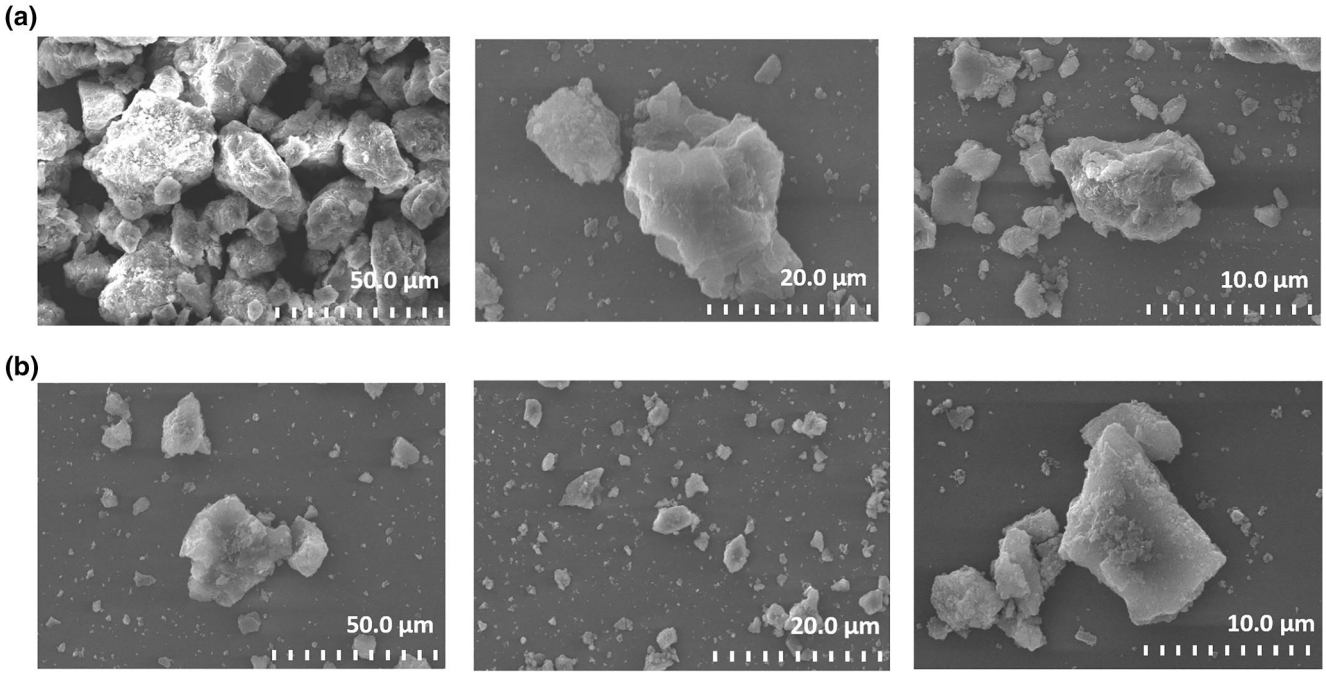

FIGURE 9 SEM images of the packed bed Al_2O_3 pellets. (a) 2 mm fresh Al_2O_3 and (b) 2 mm spent Al_2O_3

TABLE 3 Adsorption energies (E_{ad}) for the two configurations of an SF_6 molecule on different sites of the γ-Al_2O_3 (110) surface

	E_{ad} (eV)	
Site	**M1**	**M2**
1	−0.12	−0.12
2	−0.05	−0.13
3	−0.41	−0.28
4	−0.24	−0.07
5	−0.08	−0.07
6	−0.03	−0.08
7	−0.09	−0.16
8	−0.12	−0.15

visualisation. We studied two initial SF_6 configurations. In the first one, the F–S–F bond is in a straight line perpendicular to the γ-Al_2O_3 surface, which is denoted as M1 type. In the other one, the bottom 2 F atoms are parallel to the γ-Al_2O_3 surface, which is denoted as M2 type. The calculated adsorption energy E_{ad} for the two configurations at different sites are listed in Table 3.

As shown in Table 3, the values of E_{ad} of the SF_6 molecule on the γ-Al_2O_3 (110) surface are relatively low. Both M1 and M2 types have the most stable adsorption at site '3', with E_{ad} of −0.41 eV and −0.28 eV, respectively. This site is Al_{III}, corresponding to the Lewis acidic site, which is a typical active site on the surface of γ-Al_2O_3 [36]. The configurations before and after adsorption are shown in Figure 10. The E_{ad} values in the other sites are smaller, less than −0.24 eV in M1 and −0.16 eV in M2.

As shown in Figure 10, at the Al_{III} site, the SF_6 molecule has no obvious deformation after the adsorption, without a bond-breaking phenomenon. In the M1-3 configuration, the bottom F atom is close to the Al_{III} atom, and a weak bonding process occurs. However, this is not the case for the M2 configuration. In addition, after the adsorption, the bottom S–F bond length increases from 1.613 Å to 1.695 Å in the M1 configuration and to 1.629 Å in the M2 configuration. We can conclude that Al_{III} is the most stable site, at which SF_6 has a weakly chemical bonding process. While at other sites, SF_6 only has physisorption without an obvious bonding phenomenon. Figure 11 shows the differential charge distribution of SF_6 on the γ-Al_2O_3(110) surface before the bond-breaking, where the yellow and cyan regions indicate an increase and decrease in charge density, respectively. At the surface Al_{III} site, changes in the charge density prove that the electron transfer occurs between the surface atoms and the adsorbed species, which could be the main reason for stretching of the S–F bond and the activation of SF_6.

To see the degradation reaction characteristics of SF_6 over the γ-Al_2O_3 surface, we calculated the initial bond-breaking processes of SF_6 on the perfect γ-Al_2O_3 surfaces, as well as in the gas phase. The initial, TS and final configurations of the SF_6 decomposition are shown in Figure 12. The reaction occurs as follows:

$$SF_6 \rightarrow SF_5 + F \tag{5}$$

The direct S–F bond-breaking in the gas phase needs a reaction heat of 4.20 eV [37]. However, the activation energy E_a of S–F bond-breaking on the γ-Al_2O_3 surface is only 1.80 eV and it is exothermic with a reaction heat of −1.29 eV. In Figure 12, the bottom F atom decomposes from the SF_6 and binds with the Al_{III} site. The SF_5* species bind with a

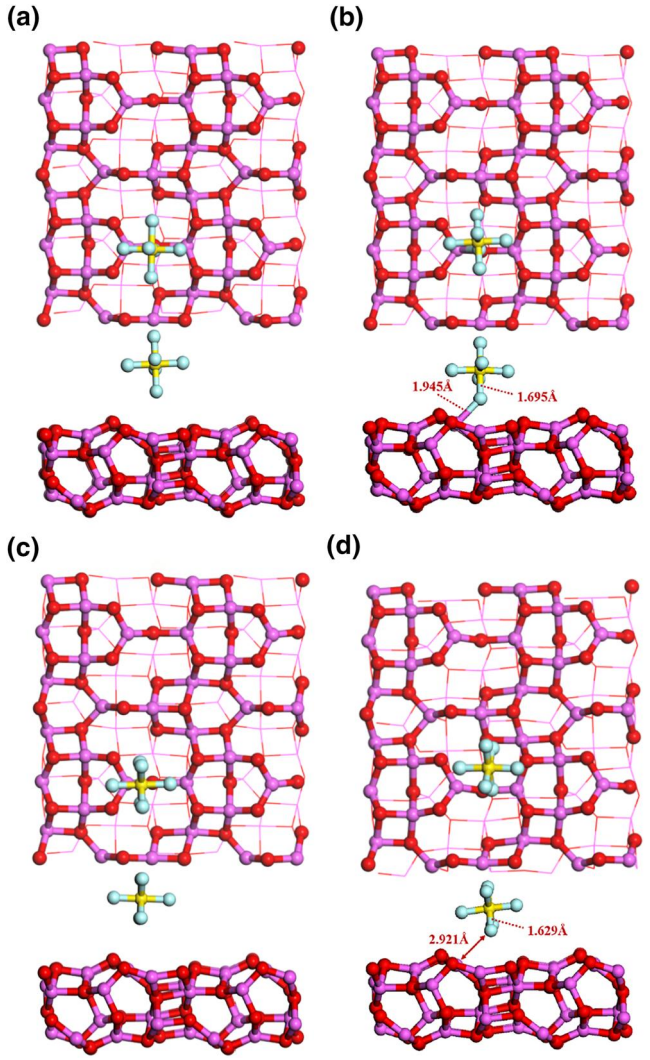

FIGURE 10 SF_6 adsorption on a perfect γ-Al_2O_3(110) surface at Al_{III} site before and after the adsorption, for two different configurations of the SF_6 molecule (Al, O, S and F atoms are in colour of pink, red, yellow and cyan, respectively. M1 and M2; see text). (a) M1-3 before adsorption, (b) M1-3 after adsorption, (c) M2-3 before adsorption and (d) M2-3 after adsorption

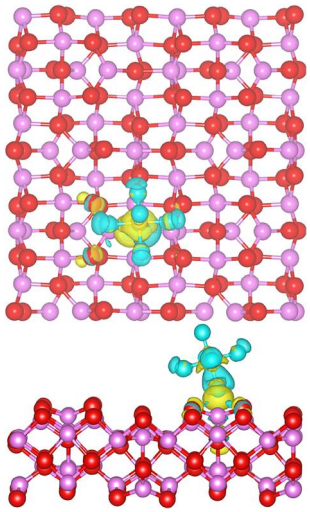

FIGURE 11 The differential charge distribution of SF_6 on the γ-Al_2O_3(110) surfaces before the bond-breaking. The yellow region indicates an increase in charge density and the cyan region indicates a decrease

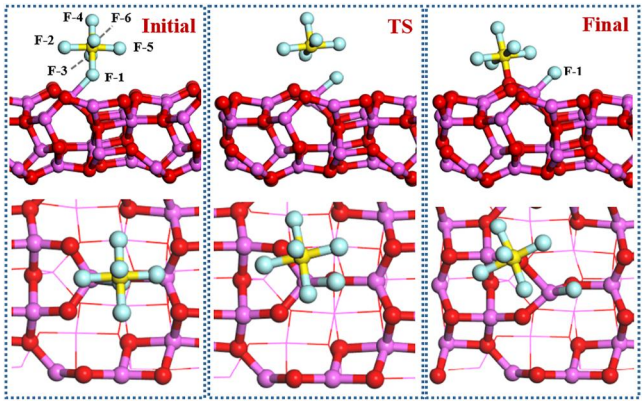

FIGURE 12 transition state(TS) process of SF_6 initial bond-breaking on the perfect γ-Al_2O_3 surface

surface O atom. This result shows that the bottom S–F bond is activated at the Al_{III} site and breaks much more easily than in the gas phase, indicating the catalytic effect of the γ-Al_2O_3 surface on SF_6 degradation. Therefore, the effective contact area of the packing is of importance for SF_6 degradation.

During the discharge, fluorine gas products such as HF, OF_2 and F_2 are generated in the plasma region and may participate in the surface reactions or be removed through the gas flow. To investigate their reaction potential, we calculated their adsorption configurations on the γ-Al_2O_3 surface, as shown in Figure 13. The E_{ad} of HF, OF_2 and F_2 are −2.54, −3.94 and −1.85 eV, respectively, all of which have obvious bonding phenomena, corresponding to the chemical adsorption. All three molecules decompose during the adsorption and form stable adsorption structures on the surface. This indicates that the fluorine gas products are reactive and are likely to react with the γ-Al_2O_3 surface to form the adsorbed F-containing species, which could be a main reason for the F element appearance of the pellet surface.

Overall, the packing size determines the gas residence time, active contact area and the discharge properties, which jointly affect the degradation behaviour. For the reactor (gap distance = 6 mm) in this study, 2 mm diameter and 1/3 of the gap distance are the optimal γ-Al_2O_3 pellet size and ratio for DRE and EY. However, due to the variation of reactor structure, packing material type and input parameters, this empirical conclusion may not suit in other DBD systems. However, the experimental results in this paper can give a qualitative reference on choosing the packing size, for both the discharge properties and the SF_6 degradation performance.

As for the product selectivity, lowering the packing size and increasing the input power promote the discharge intensity, leading to a more efficient SF_6 degradation so that the SO_2 production increases and the S-O-F gas production decreases. Our XPS test and DFT calculation reveal that the γ-Al_2O_3 surface has the catalytic effect for SF_6 activation and

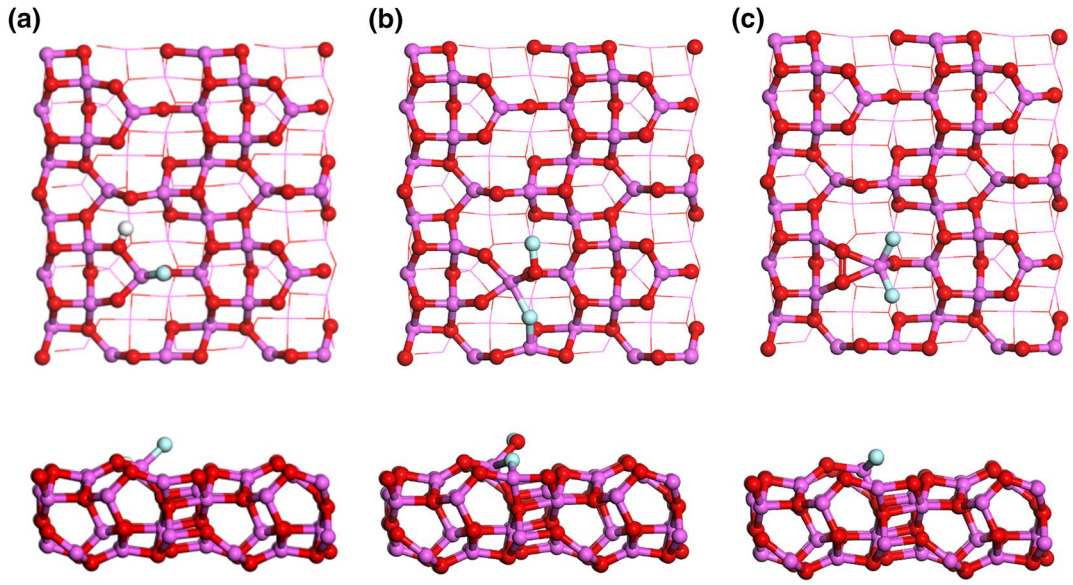

FIGURE 13 Adsorption configurations of the fluorine gas products on the γ-Al_2O_3 (110) surface. (a) HF, (b) OF_2 and (c) F_2

decomposition. Meanwhile, part of the pellets is involved in the degradation reactions, leading to a change in the surface properties. From Figure 8 we may tell that the packing method alone cannot thoroughly eliminate the S-O-F production. Reactive gases such as H_2O, O_2 and H_2 as well as the metal loading (M/γ-Al_2O_3) should be taken into consideration for the regulation of the SF_6 degradation pathway. In this case, the synergistic effects of reactive gases and packing materials should be investigated, to see how the additional gases impact the packing surface and how they jointly change the degradation reactions.

4 | CONCLUSIONS

In this study, effects of the γ-Al_2O_3 packing size and the surface properties on SF_6 degradation in a PB-DBD system are investigated by both experimental and theoretical methods. 1, 2 and 4 mm diameter γ-Al_2O_3 pellets are tested for the discharge properties and degradation performance. The results show that decreasing the packing size enhances the micro-discharges and promotes the plasma generation, leading to higher DRE and EY at a low power range of 50–80 W. However, the gas residence time becomes dominant for DRE and EY when the input power exceeds 80 W. In this system, the 2 mm pellet is the optimal size to gain the highest DRE and EY distribution, reaching a maximum EY of 34.82 g/kWh at 300 mL/min. Lowering the packing size could promote the generation of SO_2 while reducing the production of S-O-F gases, which is attributed to the improvements in the active contact area and the intensity of plasma species. At 80 W input power, the 1 mm packing system shows the highest SO_2 selectivity among the three packing systems, yielding a value of 68.29%.

BET, XPS and SEM tests of the pellet samples prove that the surface structure and properties of the γ-Al_2O_3 are affected by the discharge and degradation process. The surface area is slightly reduced and becomes smoother after the discharge, while 3.16% F and 0.49% S appear at the 2 mm sample surface after 3 h degradation. DFT results show that the SF_6 molecule can be adsorbed at the Al_{III} site over the γ-Al_2O_3 (110) surface with the bottom S–F bond elongation from 1.613 Å to 1.695 Å. The activation barrier of S–F bond-breaking is 1.80 eV over the γ-Al_2O_3 (110) surface and it is much lower than for direct decomposition in the gas phase, which has a reaction heat of 4.20 eV. F-containing gases such as HF, OF_2 and F_2 can decompose without a barrier and become stably adsorbed on the γ-Al_2O_3 surface, which could be a main reason for the surface regulation of the pellets.

In general, γ-Al_2O_3 pellets are a potential packing material for DBD treatment of SF_6 waste gases. Its surface has a catalytic effect for SF_6 activation and decomposition. The size of γ-Al_2O_3 pellets is an important factor in determining the degradation parameters, in terms of DRE, EY and product selectivity. This study gives a qualitative reference and theoretical support for the use of γ-Al_2O_3 pellets and determination of its size when considering both discharge behaviour and degradation performance.

ACKNOWLEDGEMENTS

The computational resources and services used in this work were provided by the HPC core facility CalcUA of the Universiteit Antwerpen, and VSC (Flemish Supercomputer Centre), funded by the Research Foundation - Flanders (FWO) and the Flemish Government.

CONFLICT OF INTEREST

The author declares that there is no conflict of interest that could be perceived as prejudicing the impartiality of the research study reported.

DATA AVAILABILITY STATEMENT

Data sharing not applicable to this article as no datasets were generated or analysed during the current study.

ORCID

Zhaolun Cui https://orcid.org/0000-0002-1027-1563

REFERENCES

1. Zeng, F., et al.: SF_6 decomposition and insulation condition monitoring of GIE: a review. High Volt. 6(6), 955–966 (2021)
2. Yang, Y., et al.: Review of the decomposition characteristics of eco-friendly insulation gas. High Volt. 6(5), 733–749 (2021)
3. Fang, X., et al.: Sulfur hexafluoride (SF_6) emission estimates for China: an inventory for 1990–2010 and a projection to 2020. Environ. Sci. Technol. 47(8), 3848–3855 (2013)
4. Christophorou, L.G., Olthoff, J.K., Van Brunt, R.J.: Sulfur hexafluoride and the electric power industry. IEEE Electr. Insul. Mag. 13(5), 20–24 (1997)
5. Kashiwagi, D., et al.: Metal phosphate catalysts effective for degradation of sulfur hexafluoride. Ind. Eng. Chem. Res. 48(2), 632–640 (2009)
6. Zhang, J., et al.: Efficient removal of sulfur hexafluoride (SF_6) through reacting with recycled electroplating sludge. Environ. Sci. Technol. 47(12), 6493–6499 (2013)
7. Song, X., et al.: Photodegradation of SF_6 on polyisoprene surface: implication on elimination of toxic byproducts. J. Hazard Mater. 168(1), 493–500 (2009)
8. Yamada, Y., Tamura, H., Takeda, D.: Photochemical reaction of sulfur hexafluoride with water in low-temperature xenon matrices. J. Chem. Phys. 134(10), 104302 (2011)
9. Govindan, M., Gopal, R.A., Moon, I.S.: Electrochemical sequential reduction and oxidation facilitates the continual ambient temperature degradation of SF_6 to nontoxic gaseous compounds. Chem. Eng. J. 382, 122881 (2020)
10. Gutierrez, Y., et al.: Sustainable and tunable Mg/MgO plasmon-catalytic platform for the grand challenge of SF_6 environmental remediation. Nano Lett. 20(5), 3352–3360 (2020)
11. Zhang, X., et al.: Recent advances in decomposition of the most potent greenhouse gas SF_6. Crit. Rev. Environ. Sci. Technol. 47(18), 1763–1782 (2017)
12. Cui, Z., et al.: Plasma-assisted abatement of SF_6 in a dielectric barrier discharge reactor: investigation of the effect of packing materials. J. Phys. D Appl. Phys. 53(2), 025205 (2019)
13. Bogaerts, A., et al.: The 2020 plasma catalysis roadmap. J. Phys. D Appl. Phys. 53(44), 443001 (2020)
14. Shao, T., et al.: Atmospheric-pressure pulsed discharges and plasmas: mechanism, characteristics and applications. High Volt. 3(1), 14–20 (2018)
15. Li, J., et al.: Revealing the active sites of the structured Ni-based catalysts for one-step CO2/CH4 conversion into oxygenates by plasma-catalysis. J. CO2 Util. 52, 101675 (2021)
16. Wang, L., et al.: Atmospheric pressure and room temperature synthesis of methanol through plasma-catalytic hydrogenation of CO_2. ACS Catal. 8(1), 90–100 (2018)
17. Shang, K., et al.: Successive treatment of benzene and derived byproducts by a novel plasma catalysis-adsorption process. J. Environ. Chem. Eng. 9(4), 105767 (2021)
18. Kasinathan, P., et al.: Plasma-enhanced methane direct conversion over particle-size adjusted MO_x/Al_2O_3 (M= Ti and Mg) catalysts. Plasma Chem. Plasma Process. 34(6), 1317–1330 (2014)
19. Butterworth, T., Elder, R., Allen, R.: Effects of particle size on CO_2 reduction and discharge characteristics in a packed bed plasma reactor. Chem. Eng. J. 293, 55–67 (2016)
20. Wang, B., et al.: Improvement of the activity of CO_2 methanation in a hybrid plasma-catalytic process in varying catalyst particle size or under pressure. J. CO2 Util. 46, 101471 (2021)
21. Zhang, X., et al.: Effects of background gas on sulfur hexafluoride removal by atmospheric dielectric barrier discharge plasma. AIP Adv. 6(11), 115005 (2016)
22. Manley, T.C.: The electric characteristics of the ozonator discharge. Trans. Electrochem. Soc. 84(1), 83 (1943)
23. Peeters, F.J.J., Van de Sanden, M.C.M.: The influence of partial surface discharging on the electrical characterization of DBDs. Plasma Sources Sci. Technol. 24(1), 015016 (2014)
24. Kurte, R., et al.: Application of infrared spectroscopy to monitoring gas insulated high-voltage equipment: electrode material-dependent SF_6 decomposition. Anal. Bioanal. Chem. 373(7), 639–646 (2002)
25. Hutter, J., et al.: cp2k: atomistic simulations of condensed matter systems. Wiley Interdiscip. Rev. Comput. Mol. Sci. 4(1), 15–25 (2014)
26. VandeVondele, J., Hutter, J.: Gaussian basis sets for accurate calculations on molecular systems in gas and condensed phases. J. Chem. Phys. 127(11), 114105 (2007)
27. Perdew, J., Burke, K., Ernzerhof, M.: Generalized gradient approximation made simple. Phys. Rev. Lett. 77(18), 3865 (1996)
28. Grimme, S., et al.: A consistent and accurate ab initio parametrization of density functional dispersion correction (DFT-D) for the 94 elements H-Pu. J. Chem. Phys. 132(15), 154104 (2010)
29. Head, J., Zerner, M.: A Broyden—Fletcher—Goldfarb—Shanno optimization procedure for molecular geometries. Chem. Phys. Lett. 122(3), 264–270 (1985)
30. Henkelman, G., Uberuaga, B.P., Jónsson, H.: A climbing image nudged elastic band method for finding saddle points and minimum energy paths. J. Chem. Phys. 113(22), 9901–9904 (2000)
31. Cui, Z., et al.: Plasma-catalytic methanol synthesis from CO_2 hydrogenation over a supported Cu cluster catalyst: insights into the reaction mechanism. ACS Catal. 21, 1326–1337 (2022)
32. Wang, W., et al.: Streamer propagation in a packed bed plasma reactor for plasma catalysis applications. Chem. Eng. J. 334, 2467–2479 (2018)
33. Tsai, W.T.: The decomposition products of sulfur hexafluoride (SF_6): reviews of environmental and health risk analysis. J. Fluor. Chem. 128(11), 1345–1352 (2007)
34. Zhong, L., et al.: Theoretical study of the chemical decomposition mechanism and model of Sulfur hexafluorid (SF_6) under corona discharge. J. Fluor. Chem. 220, 61–68 (2019)
35. Zhang, J., et al.: Photocatalytic and degradation mechanisms of anatase TiO_2: a HRTEM study. Catal. Sci. Technol. 1(2), 273–278 (2011)
36. Bal, K.M., et al.: Effect of plasma-induced surface charging on catalytic processes: application to CO_2 activation. Plasma Sources Sci. 27(2), 024001 (2018)
37. Chase, M.W.: NIST-JANAF thermochemical tables 2 Volume-set. (Journal of Physical and Chemical Reference Data). American Institutes of Physics (1998)

SUPPORTING INFORMATION

Additional supporting information can be found online in the Supporting Information section at the end of this article.

How to cite this article: Cui, Z., et al.: SF_6 catalytic degradation in a γ-Al_2O_3 packed bed plasma system: A combined experimental and theoretical study. High Voltage. 1–11 (2022). https://doi.org/10.1049/hve2.12230